Acta Oceanol. Sin., 2017, Vol. 36, No. 11, P. 4–13
DOI: 10.1007/s13131-017-1120-1
http://www.hyxb.org.cn
E-mail: hyxbe@263.net

The spatio-temporal variation of wintertime subtidal currents in the western Taiwan Strait

SHEN Junqiang[1], QIU Yun[1, 2*], GUO Xiaogang[1], PAN Aijun[1], ZHOU Xiwu[1]

[1] Third Institute of Oceanography, State Oceanic Administration, Xiamen 361005, China

[2] Laboratory for Regional Oceanography and Numerical Modeling, Qingdao National Laboratory for Marine Science and Technology, Qingdao 266237, China

Received 27 March 2017; accepted 4 May 2017

Abstract

A new data set of observations by six cruises of ship-mounted acoustic doppler current profiler (SADCP) and three 40 d long bottom-mounted ADCPs (BADCPs) is employed to reveal the spatiotemporal variability of tidal and subtidal currents in the western Taiwan Strait (TWS) during winter season. The results confirm the existence of intense cotidal lines for M_2 tidal current, which is located north of 25°N. In this case, no existence of an amphidromic point can be identified. It is also revealed that the counter-wind current (CWC) can extend through the whole western TWS and even occupy the entire water column during winter monsoon relaxation. However, this CWC is observed to be thoroughly overwhelmed by the downwind China coastal current (CCC) during the two big monsoon bloom events in the winter of 2007, and the CCC consequently extends southward throughout the western TWS instead. Most importantly, the variation of the spatial extent for the CWC and the CCC in the western TWS is found to be well explained by the first two modes of the vector empirical orthogonal function (VEOF) analysis, that is, it is mainly controlled by a wind-driven quasi barotropic current as the first mode and slightly modulated by a relatively weak background current with a first-order baroclinic structure as the second mode.

Key words: counter-wind current, China coastal current, M_2 tidal current, Taiwan Strait, winter season

Citation: Shen Junqiang, Qiu Yun, Guo Xiaogang, Pan Aijun, Zhou Xiwu. 2017. The spatio-temporal variation of wintertime subtidal currents in the western Taiwan Strait. Acta Oceanologica Sinica, 36(11): 4–13, doi: 10.1007/s13131-017-1120-1

1 Introduction

The Taiwan Strait (TWS), located between the East China Sea and the South China Sea, is a crucial passage for water and nutrient exchange between these two sea areas. The strait is generally shallower than 60 m except for the deep Penghu Channel, and is characterized by a complex bottom topography. The circulation in the TWS, primarily forced by monsoons, the bottom topography and remote forces (e.g., the South China Sea Warm Current and the Kuroshio branch current in the eastern TWS), shows a significant seasonal variation (Guan and Fang, 2006; Hu et al., 2010).

Unlike summertime when the entire strait is occupied by uniform northward/northeastward flows, the wintertime circulation is much more complicated with several unique flows. The Taiwan Strait Warm Current proposed in the pioneering work of Guan (1986) and Guan and Fang (2006) is actually a counter-wind current (hereinafter CWC), which originates from the sea off Guangdong Province, China as an extension of the South China Sea Warm Current and connects with the Taiwan Warm Current north of the strait. The follow-up studies using *in situ* observations (Chuang, 1986; Hu et al., 1990) and numerical models (Su and Wang, 1987; Wang et al., 2010) confirmed the existence of the CWC. Although the spatial extent of the CWC on the surface and intermediate layers changes greatly in response to the intraseasonal variation of local wind during winter (Guan and Fang., 2006; Hu et al., 1990), the current in the bottom layer is stable throughout the whole western TWS (Zhang et al., 1991; Sun et al., 1996). The northeastward pressure gradient along the western boundary is proposed as the main forcing mechanism for the CWC (Chuang, 1985; Yang, 2007).

Another important current in the western TWS during wintertime is the China coastal current (CCC), which is a downwind coastal current located closely adjacent to the landward side of the CWC (Jan et al., 2002; Zhang et al., 2005; Hu et al., 2010). It carries colder and less saline coastal water southward and extends as far as to Nan'ao Island in Guangdong Province (Xiao and Cai, 1988). During the cold-air outbreak, the CCC was reported to intrude southeastward into the Penghu Island area from the western strait (Liao et al., 2013). Hydrographic observations suggested that the interannual variation of this downwind current was significant; the strength and spatial extent of this current are largely enhanced (reduced) under strengthened (weakened) northeast monsoon during La Niña (El Niño) events (Wu et al., 2007; Zhu et al., 2013). The monsoon forcing (Chen,

Foundation item: The National Natural Science Foundation of China under contract Nos 41506014, 41306027 and 41276034; the Scientific Research Foundation of Third Institute of Oceanography, State Oceanic Administration under contract No. 2017011; the State Oceanic Administration Program on Global Change and Air-Sea Interactions under contract Nos GASI-IPOVAI-02, GASI-IPOVAI-03 and GASI-03-01-01-04; the Chinese Academy of Sciences Strategic Leading Science and Technology Projects under contract No. XDA1102030104.

*Corresponding author, E-mail: qiuyun@tio.org.cn

2003; Zhang et al., 2005; Jan et al., 2006) and the coastally trapped waves that propagate southward (Ko et al., 2003; Pan et al., 2013) are considered as two major driving mechanisms of the CCC.

During the past decade, many studies contributed to the understanding of wintertime current characteristics in the TWS based on various valuable observations, including bottom-mounted and ship-mounted acoustic doppler current profilers (hereinafter BADCP and SADCP, respectively) (Liang et al., 2003; Wang et al., 2003; Lin et al., 2005), surface drifters (Tseng and Shen, 2003; Qiu et al., 2011) and high-frequency ground wave radars (Zhu et al., 2013). However, most of the *in situ* current data during winter were obtained under calm sea conditions; the data under rough sea conditions are rarely available. It is still difficult to explicitly depict the spatial pattern of current response to the evolving northeasterly wind.

In this study, we mainly focus on the flow field response to an evolving winter monsoon in the western TWS using a set of new *in situ* data obtained under both calm and strong wind conditions. The remainder of this paper is organized as follows: in Section 2, we describe the data and the analytical methods used in this study; in Section 3, we present the features of tidal currents; in Section 4, we analyze the variation of subtidal currents as a response to varying local wind; and a summary is provided in Section 5.

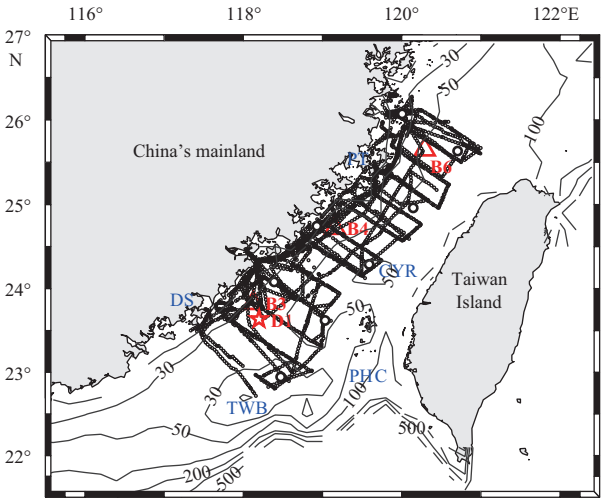

Fig. 1. Bathymetric chart (contours in m) of areas around Taiwan. The cruise tracks of the SADCP observations from 2005 to 2012 are denoted by the dotted lines. Three BADCP stations and the mooring buoy are marked by the red triangles and a red star, respectively. The black circles denote the nodes, and the solid lines are isobaths. The major geographic locations involved in this paper are labeled, including the Changyuen Ridge (CYR), the Penghu Channel (PHC), the Taiwan Bank (TWB), Pingtan (PT) and Dongshan (DS) Island, etc.

2 Data and methods

2.1 *Data*

The SADCP current data used in this study were collected in the winter seasons from 2005 to 2012. During the study period, there were six cruises in total, out of which three lasted for more than 10 d (Fig. 1 and Table 1). The ship velocity was calculated from the bottom tracking, and was deducted from the raw SADCP data by using the data processing software VmDas. The average time interval of the data was 5–10 min, and two types of frequencies were set up for the current-profiler observations, with a bin length of 2 m for 300-k ADCP and of 4 m for 150-k ADCP. Three criteria were used to characterize the acceptable data, namely, the percentage of good data should be greater than 50%, the error of the velocity and the vertical velocity should be less than 0.15 m/s, and the ship speed should be slower than 6 m/s. Linear interpolation was then used to fill the gaps in the acceptable profiles. Subtidal currents were extracted from depth-averaged SADCP data following the method of Candela et al. (1992), which are used to analyze the spatial pattern of winter currents.

Three BADCPs (i.e., B3, B4 and B6 in Fig. 1), which were located at water depths of 41, 41 and 43 m respectively, were deployed in the western TWS during 3 December 2007 to 12 January 2008. Current velocity profiles and near-bottom temperature were measured at each mooring. Given the ADCP installation height (beams surface from the seabed being about 0.5 m) and the resulting blind zone (upper 2.5 m), the deepest current observations were about 5 m above the seabed. The valid measured depth nearest to the sea surface was 4 m, because the near-surface bins were contaminated by side-lobe reflection from the sea surface. Then, the current velocity data at 4–36, 4–36 and 4–38 m were collected with a 2-m nominal bin, while the temperature was measured at 40.5, 40.5 and 42.5 m for B3, B4 and B6, respectively. All moorings were recovered successfully with record lengths of about 40 d and ensemble averaged at a time interval of 1 h. To exclude high-frequency fluctuations of semidiurnal and diurnal tidal currents from the velocity observed, a digital symmetric low-pass filter (i.e., PL33) (Limeburner, 1985) was applied to removing the fluctuations with periods less than 33 h. Similarly, the temperature data were smoothed by 11-point running average to reduce the noise. The filtered current velocity (which is the subtidal current) together with the filtered temperature data are used to explore the vertical structure of currents in the western TWS.

For surface wind, we used hourly *in situ* data from 3 December 2007 to 12 January 2008 collected by the mooring buoy D1, positioned closely to B3 (Fig. 1). Before analysis, high-frequency fluctuations in the wind speed data were filtered out by applying the same low-pass filter employed in processing the current velocity of the BADCPs. Furthermore, the 6-hourly ERA-40 reanalysis wind velocity field (with a speed bias of 1.36 m/s and a direction

Table 1. The information of SADCP current data set

Year	Time (data range)	Version	Instrument setup		
	Month (Day)		Bin size/m	First bin depth/m	Ensemble interval/min
2005	Mar. (7–17)	WHM-300k	2	7	10
2006/2007	Dec. (24–31), Jan. (1–10, 14–16, 19–31), Feb. (3–6)	WHM-300k	2	7	5
2007/2008	Dec. (1–4), Jan. (5–8)	WHM-300k	2	7	5
2007	Dec. (10–22)	WHM-150k	4	15	5
2012	Feb. (20–24, 27–29), Mar. (1)	WHM-300k	2	7	5
2012	Nov. (19–20, 25)	WHM-300k	2	7	10

root-mean-square error of 33° in the TWS, as noted by Kuang et al., 2015) on 0.125° grid was also obtained by averaging in the domain from 22° to 26°N and from 117° to 121°E . The sample interval is improved to 1 h using linear interpolation, and thus the obtained data matched those of the SADCP data at every integral point. The reanalysis wind field is used to explore the wind characteristics during the period of the SADCP observations, while the *in situ* wind data are analyzed to understand the response characteristics of subtidal currents to the short-term fluctuations of winter monsoon.

2.2 *Least squares method*

As intense tidal currents are ubiquitous in coastal and shelf waters, a snapshot of the SADCP data is unavailable when investigating the subtidal current field unless the observed current is detided with a reliable process. Therefore, methods have been developed to remove tides from the SADCP measurements, such as the traditional harmonic analysis method (Geyer and Signell, 1990; Takikawa et al., 2003), the method based on a tidal forecasting model (Isobe et al., 2007) and the spatio-temporal fitting by the least squares method (STF-LSM) (Candela et al., 1992; Münchow, 2000; Vazquez et al., 2011). Among these methods, the STF-LSM is most widely used to separate the mean flow from tidal currents, because it can extract those spatially evolving tide currents by fitting arbitrary basis functions (Candela et al., 1992), which does not require repeated transects and hence has a logistic advantage. A brief summary of the methodology involved is presented here, while a more detailed explanation can be found in Wang et al. (2004). The fitting scheme is implemented to the vertically integrated velocity field from the SADCP measurements. The irregularly sampled (both in space and time) velocity components are represented as follows:

$$u(r,t) = \sum_{k=1}^{K}\left\{\alpha_k + \sum_{j=1}^{M}\left[\beta_{jk}\cos(\omega_j t) + \gamma_{jk}\sin(\omega_j t)\right]\right\} \times \varphi(|r-r_k|) + \psi(r,t)\,, \quad (1)$$

where $u(r, t)$ is the zonal component of vertically integrated velocity at time t and given location r; $\varphi(|r–r_k|)$ is the base function; $\psi(r, t)$ is the residual term including the measurement noise and unresolved tidal constituents; α_k is the mean flow coefficient; β_{jk} and γ_{jk} are tidal component coefficients; K is the number of nodes; M is the number of tidal constituents used in the analysis; ω_j is the frequency of the jth tidal constituent; r is the location of the observations; and r_k is the kth nodal location. A similar equation is used for the meridional component $v(r, t)$.

The coefficients α_k, β_{jk} and γ_{jk} are determined by a least-squares fitting of the SADCP data using Eq. (1). In the TWS, the semidiurnal tidal current, especially the M_2 constituent, is dominant (Fang et al., 1985; Jan et al., 2004). Since it is difficult to separate M_2 from other semidiurnal tides like S_2, N_2 and K_2 because the duration of each individual cruise was relatively short, only M_2 is considered in Eq. (1) (i.e., M=1) in this study. A simple Gaussian interpolation function proposed by Wang et al. (2004) is selected as the spatial basis function as shown as follows:

$$\varphi(|r-r_k|) = \exp(-|r-r_k|^2/2L^2), \quad (2)$$

where L is the space impact factor intimately associated with a node-affected area. Since the spatial weighting of the Gaussian function decreases with increasing distance, the interpolation is dominated by local influence from nearby data points. Here, the number of node is assumed to be 8 and the space impact factor is set to 110 km. The distribution of the nodes is shown in Fig. 1. Though the tidal currents and the mean flow in the study area vary spatially and the observation errors are random in the SADCP data, the results from this calculation are not sensitive to the distribution of nodes.

2.3 *Barotropic tidal model*

To evaluate the tidal currents extracted from the SADCP measurements, a two-dimensional barotropic coastal tidal model, named ADCIRC (Westerink et al., 1993), is used. The model foring term is obtained from the tidal potential that is derived from eastern China's seas using the Oregon State University tidal model (TPXO) with eight tidal constituents (i.e., K_1, K_2, M_2, N_2, O_1, P_1, Q_1, and S_2). In the computation, the unstructured grids are employed, and the global bathymetry is subsampled from 1′ gridded earth topography (ETOPO1) data.

This model reproduces the M_2 tidal ellipse parameters obtained from the BADCP measurements at B3, B4 and B6 very well (Table 2), though the observation results (e.g., the major axis of M_2 ellipse) are biased upward as they do not resolve all the semidiurnal tidal components due to the short time span of just 40.2 d. Overall, the excellent agreement between the ADCIRC model results and the BADCP measurements demonstrated that the true M_2 currents could be well represented by the modeled M_2 tidal constituent in the TWS.

3 Tidal currents

Figure 2a shows the M_2 tidal current ellipses obtained from the SADCP observations and calculated from the ADCIRC model output. Within most of the region of our concern, both tidal ellipses were quite similar in terms of current speed, direction, phase, ellipticity, and rotation. The averaged value (0.44 m/s) of the maximum tidal current amplitude by the SADCP observations is rather close to that (0.43 m/s) given by the ADCIRC model, and the correlation coefficient between them is 0.73 with a standard deviation of 0.13 m/s. Obviously, with sufficient data, the SADCP-derived M_2 tidal current should be rather reliable, whose accuracy is at least comparable to that from the ADCIRC model. Consistent with previous studies (Fang et al., 1985; Wang et al., 2003; Jan et al., 2004), both SADCP and model results (Fig. 2a) show that the inclination of M_2 ellipses is generally in the NE–SW direction, which is thought to be primarily constrained by isobaths, but it turns into the NW–SE direction in the shallow Taiwan Bank and the northwest Penghu Channel. Though the model results agree well with the observations in general, we

Table 2. The elements of tidal ellipses of M_2 constituent obtained in the observation and the numerical tide model (abbreviated as Obs and Mod, respectively) at three current stations

Station	Major axis/cm·s^{-1}		Small axis/cm·s^{-1}		Inclination/(°)		Phase/(°)	
	Obs	Mod	Obs	Mod	Obs	Mod	Obs	Mod
B6	33.8	35.0	23.8	14.9	48	73	86	60
B4	32.2	26.0	14.1	13.4	27	17	195	199
B3	45.7	36.9	2.9	7.3	44	42	232	215

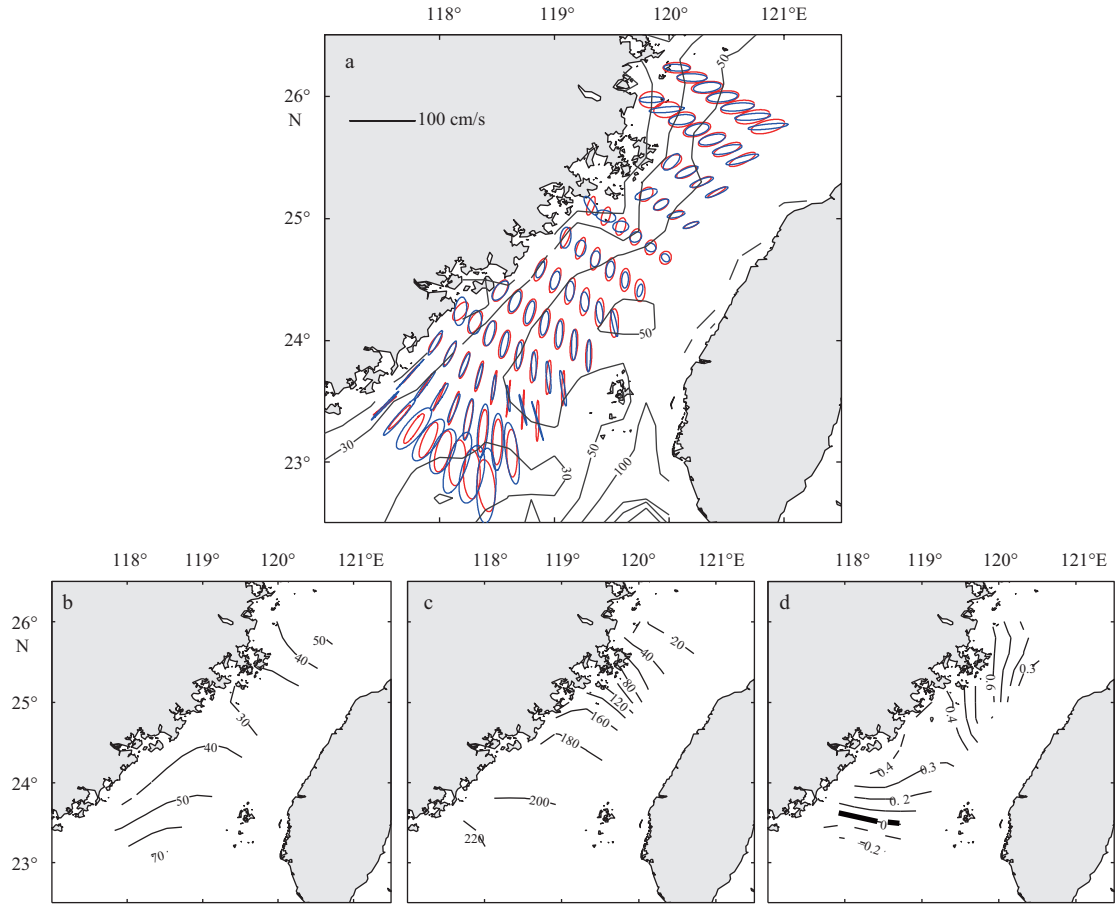

Fig. 2. The barotropic tidal current ellipses (M_2) derived from the SADCP data (red) and the barotropic tidal model (blue) (a); and co-amplitude (cm/s) (b), co-phase (°) lines (subject to time of 120°E) (c) and ellipticity (d) for M_2 constituent derived from the SADCP data. The bold line in Fig. 2d represents the boundary of different rotation motions of M_2 currents.

should mention that in some places, e.g., the TWS center close to the mainland coast and the northwest Taiwan Bank, the model results of ellipse inclination deviate away from the measured ones. This deviation is probably because the model can adjust well with the changing isobaths on the premise of not missing local fluctuations; meanwhile, the STF-LSM that emphasizes the smoothness of interpolation (Münchow, 2000) probably neglects the fluctuations of local signals (Chiao and Wang, 2004).

Figures 2b–d reveal several major characteristics of the M_2 tidal current. One can see that the strong tidal currents appeared near the two ends of the TWS and diminished gradually towards the central strait (Fig. 2b). The maximum M_2 current amplitude is about 0.8 m/s on the Taiwan Bank (22.8°N, 118.4°E), whereas its minimum amplitude is less than 0.3 m/s in the central strait. From the co-phase lines for M_2 currents (Fig. 2c), it is found that the maximum velocity first appeared in the northeastern part and then propagated southward. This result is consistent with the harmonic analysis of sea level records (Jan et al., 2004), suggesting that the M_2 tide is a progressive wave in the western TWS. Obviously, there exist intense cotidal lines north of 25°N, where the M_2 current amplitude is almost minimum (Fig. 2b). Within this region, the time difference between the north and the south is about 3 h (about 90°). This was also reported in previous studies (e.g., Fang et al., 1985; Li and Wang, 1990). However, no amphidromic point proposed by Ye et al. (1985) is found in our study. From the distribution of the M_2 ellipticity shown in Fig. 2d, at approximately 23.5°N there exists a latitudinal 0 isoline. South of the 0 isoline there are negative values, which suggest the clockwise rotational motion of the M_2 currents, whereas the case for the north of the isoline is exactly the opposite.

4 Subtidal currents during winter monsoon

4.1 *Spatial distribution of subtidal currents during winter monsoon relaxation*

Figure 3a shows the depth-averaged mean subtidal currents over the entire SADCP observation periods and the standard deviation of residual currents. The stability of the mean subtidal currents can be examined by comparing their magnitude with their standard deviation. Generally, the standard deviation of the residual currents is significantly smaller than the mean subtidal currents, except for the situation of the mainland coast, where the two are comparable. The flow field in the western portion of the TWS is dominated by northeastward currents against the northeasterly wind (i.e., the CWC). The strong CWC is near the Changyuen Ridge (the maximum current is 0.38 m/s) and extends northward to Pingtan Island, while the weak CWC generally occurs off the mainland coast. Additionally, a very weak southwestward current was found north of Pingtan Island, which was characterized by the narrow mainstream close to the coast, and it has been reported as the CCC (Jan et al., 2002; Pan et al., 2013).

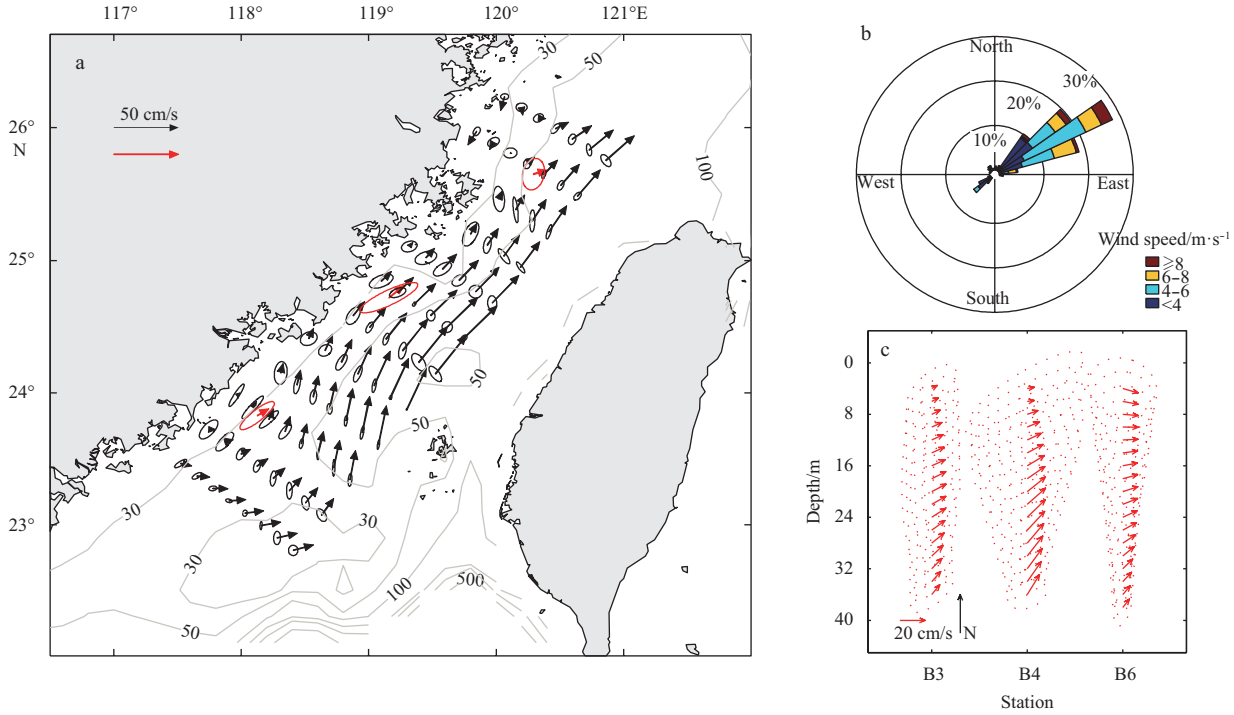

Fig. 3. The distribution of the mean subtidal currents (black arrows) over the entire SADCP observation period, the standard deviation of residual currents (black ellipses), and the mean depth-averaged subtidal currents (red arrows) with the corresponding standard deviations (red ellipses) from BADCPs' measurements obtained with sea surface wind speed less than 8 m/s (a); the rose diagram (b) was obtained from the ERA40 reanalysis sea surface wind over the same period of SADCP observations; and the same mean subtidal currents (arrows) and standard deviations (ellipses) as those in Fig. 3a, displayed with vertical levels (c).

During the SADCP observations, the northeasterly wind prevailed in the TWS, which accounted for up to 83.9% of the total surface wind samples (Fig. 3b), but the wind was generally weak, with the wind speed less than 8.0 m/s accounting for 95.2% of the total samples. In addition, the average wind speed was only about 4.6 m/s, which was far less than the general mean strength of wind (about 8.6 m/s; see Table 1 in Li (1986)) during the same winter months when the SADCP data were collected. The monsoon was considered as being in a relaxed state during the SADCP observations. Therefore, the aforementioned mean subtidal currents shown in Fig. 3a only present the spatial pattern of the flows under calm sea conditions.

The current measurements during winter monsoon relaxation stage (i.e., when the sea surface wind speed was less than 8.0 m/s) from the three BADCPs are used to reveal the vertical structure of flows in the western TWS (Figs 3a and c). Consistent with the flow pattern from the SADCP observations, the mean depth-averaged flows at all sites show primarily northeastward currents (Fig. 3a). However, by examining the major axis of the standard deviation ellipse (red and black ellipses, Fig. 3a), one can see that the magnitudes of the flow fluctuations at the three stations were all far larger than those of the SADCP observations at the corresponding locations, particularly at B4. Note that between the SADCP and BADCPs measurements, only the latter measurements can reveal the short-term variation of the flows. Therefore, the aforementioned large discrepancy in the flow variation between the BADCPs and the SADCP suggests that very strong flow components for the short-term variation existed at the three sites, which cannot be resolved by SADCP since it is a kind of irregular-sampling measurement.

Figure 3c shows the mean subtidal current profile for these three stations averaged during the winter monsoon relaxation stage. The result indicates that the mean subtidal currents for all layers at B3 and B4 are northeastward, with the maximum of each site all located in the middle level (up to 0.13 and 0.20 m/s for B3 and B4, respectively). In contrast, the mean subtidal currents at B6 are southeastward from the surface to the 8 m layer with its maximum (about 0.13 m/s) located in the surface layer, whereas it turned to northeastward in the layers below 8 m. The major axis of ellipses at B3 indicates that at this station the fluctuation amplitude is almost uniform among all layers, whereas for B4 and B6, a significant decreasing trend in the fluctuation amplitude is observed from the top to the bottom layer. The fact that the uniform northeastward flows from the middle to the bottom layers at all three sites suggests that the CWC can extend throughout the whole western strait during winter monsoon relaxation stage. However, in the surface layer, due to the dominating southeastward CCC in the northern part (i.e., the location of B6), the CWC only extended from the south to the middle part along the western strait (i.e., from the location of B3 to that of B4).

4.2 *Spatio-temporal variation of subtidal currents*

The northeast monsoon begins in mid-September and peaks from October to January in general (Jan et al., 2002). It has strong short-term variation with a period of 3–10 d induced by successive cold fronts passing over the China's continental shelf (Hsueh and Romea, 1983). Consequently, the flows in the strait are largely affected by the short-term fluctuation of winter wind. As shown in Fig. 4a, though the fluctuation of the depth-averaged flows at the three stations during the whole observation periods was as strong as that observed under calm sea conditions (see Fig. 3a), the flow patterns at all sites averaged for these two periods were quite different (Figs 4b and 3c). By comparing Fig. 4b with Fig. 3c, one can see that the CCC derived from the mean

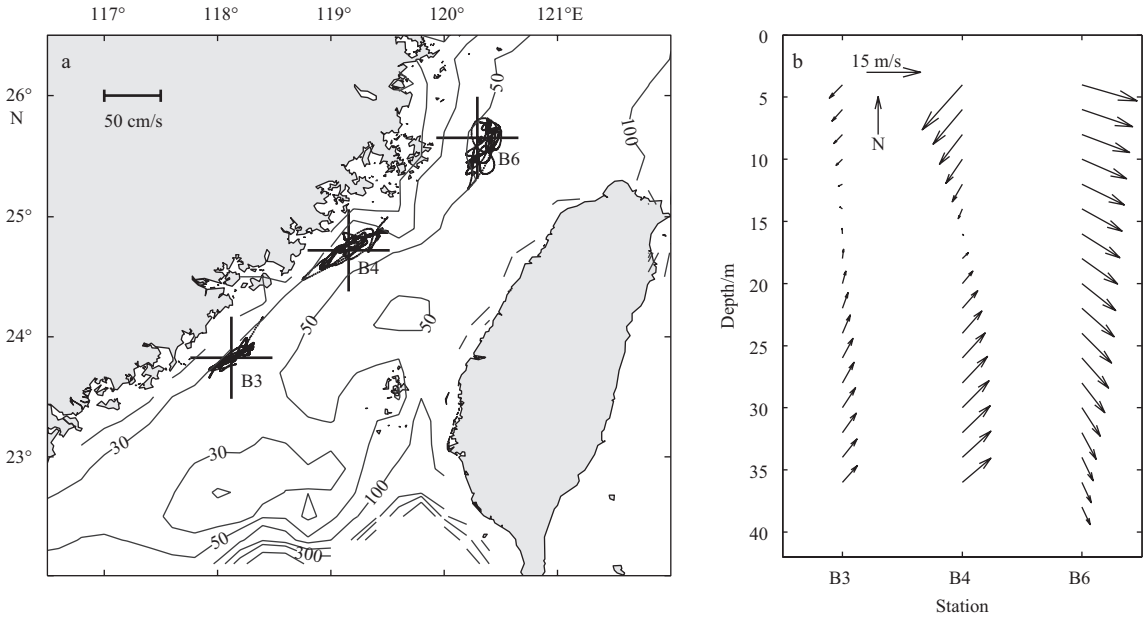

Fig. 4. Scatter diagram of depth-averaged subtidal current fluctuations at three stations superimposed on a bathymetric contour map from 3 December 2007 to 12 January 2008 (a), and the vertical distribution of mean subtidal currents at the three stations (b).

subtidal currents for the whole periods was far stronger than the counter-part obtained for the monsoon-relaxation periods. What is more, it has a larger spatial extent, which occupied the whole western strait, covering the full depth in the northern strait (i.e., at the location of B6) and the upper layers (above 16 m) in the central and southern parts (i.e., at the locations of B3 and B4). In contrast, compared with that during the monsoon relaxation stage, the strength and spatial extent of the mean CWC during the full period were dramatically reduced. As shown in Fig. 4b, the mean CWC over the whole period only appeared in the layers below 16 m in the central and southern parts of the western TWS (i.e., the locations of B4 and B3). The large difference in mean flow pattern over the aforementioned two monsoon stages suggests that the variation of the two major flows (i.e., the CWC and CCC) is sensitive to the short-term variation of the winter monsoon.

Figure 5 is a comprehensive depiction of the characteristics of the aforementioned two flows (i.e., the CWC and CCC) in response to different stages of winter monsoon (i.e., relaxation or peak stage). The *in situ* sea surface wind (Fig. 5a) indicates that the northeasterly wind prevailed in the TWS during the periods of BADCPs' measurements, with strong short-term variation. Among the short-term variation, there were four big monsoon relaxation events (shown as red-shaded areas in Fig. 5a) and two big monsoon bloom events (shown as blue-shaded areas in Fig. 5a). The mean surface wind speed during these relaxation events ranged from 1.4 to 8.0 m/s, and those during the bloom events varied from 10.0 to 15.6 m/s.

Consistent with the surface wind (Fig. 5a), the along-shore and cross-shore current components showed notable short-term fluctuations (Figs 5b–g), which were almost in phase with the variation of the surface wind. Under the intense northeasterly wind, the prevailing current direction of the alongshore component at all sites was primarily toward the southwest, while the northeastward CWC was very weak and only existed in the subsurface and bottom layers (Figs 5b–d and 5h–j). Particularly, during the two big monsoon bloom events, the whole water column at all sites was dominated by the strong southwestward CCC, and the CWC was hardly detectable (Figs 5b–d). In contrast, during the weak winter monsoon, the above processes were exactly the opposite (Figs 5b–d and 5h–j), which are consistent with those shown in Fig. 3. The northeastward CWC was evidently displayed in the whole water column of all sites for most of the big monsoon relaxation events. Although the CCC still existed at B3 and B4 during the third monsoon relaxation event, its strength was significantly weakened in the subsurface and bottom layers (Figs 5c and d).

Similar to the aforementioned alongshore current, the cross-shore current component at all sites showed nearly in-phase fluctuations with the surface wind (Figs 5e–g). It appeared to be in the onshore direction during the two monsoon bloom events, whereas it became offshore during the four monsoon relaxation events when the surface wind remained northeasterly with profoundly diminished strength in most of the cases. Within the wind-driven Ekman regime, the cross-shore sea level slope induced by the Ekman advection was formed during the wintertime monsoon outbreaks, whereas the alongshore sea level slope caused by the mighty Kuroshio (Yang, 2007) was present during the monsoon relaxation stage. Such scenarios were probably the major factors leading to the variation of the cross-shore currents.

The near-seabed temperatures at the three sites provide additional evidence for the variation of two major flows (i.e., the CWC and the CCC) in the western strait (Figs 5b–d). Overall, the temperatures rose during the monsoon relaxation stage. At Station B6, which was located in the northern TWS, the temperature rose from ~18 to 21°C on 23 December 2007 when the northeasterly wind weakened. The warm water carried by the extension of the CWC to the north of Pingtan Island probably contributed to the rising of the temperature at B6 (Pan et al., 2013). When the monsoon was persistently intensified (e.g., the second monsoon bloom period), the CWC almost disappeared from the western strait. Consequently, instead of warm water, the southward extension of the cold coastal water was brought in by the CCC along the whole western strait, which resulted in a 4.0–5.0°C decrease in bottom water temperature at B6. The nearly identical variation of the near-seabed temperature with smaller amplitude than that of B6 was detected at B4. Nonetheless, the near-seabed temperature of B3, which was located in the southern strait, re-

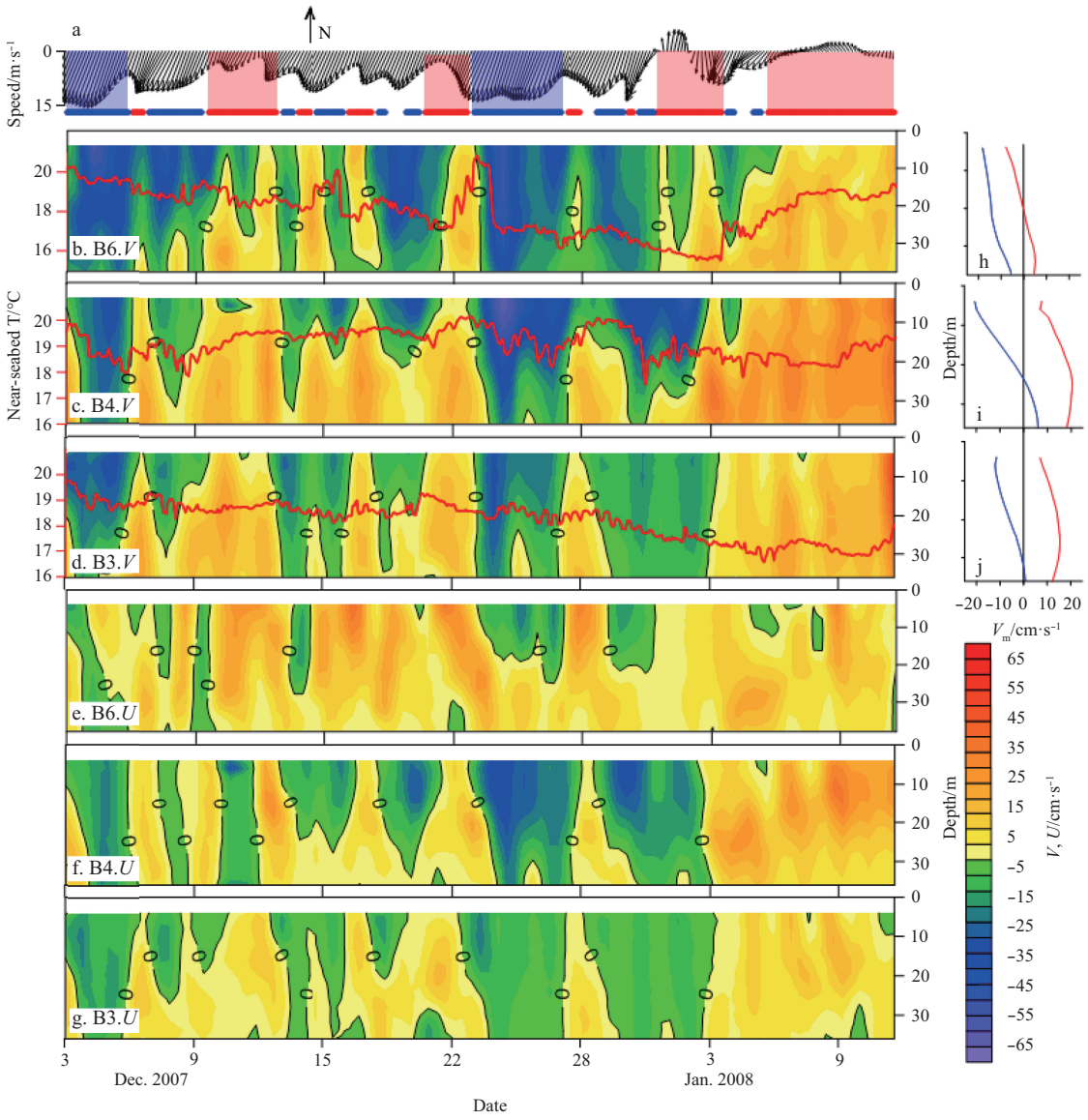

Fig. 5. Sea surface wind vectors (a). The red (blue) solid line corresponds to the period of monsoon wind speed less than 8 m/s (larger than 10 m/s), and the red (blue) shadow covers the time axis during the monsoon relaxation (prevalent), which are displayed at the top. The vertical profile of alongshore subtidal speed V (whose positive and negative values correspond to the northeast and southwest directions, respectively) at B6 (b), B4 (c) and B3 (d); and the synchronous near-seabed temperature T is shown. The vertical profile of cross-shore subtidal speed U (whose positive and negatives values corresponds to the offshore and onshore directions, respectively) at B6 (e), B4 (f) and B3 (g). The vertical distribution of mean $V(V_m)$ is displayed by the red lines (blue lines) at B6 (h), B4 (i) and B3 (j), under the condition of sea surface wind speed less than 8 m/s (larger than 10 m/s) at the top. Note that, the so-called "principal" coordinate system proposed by Kundu and Allen (1976) is used to divide the subtidal current into the alongshore and cross-shore components, and the relevant principal directions calculated are 33°, 27° and 12° for B3, B4, B6, respectively. After clockwise rotation of the Cartesian coordinate by the above principal directions, the alongshore current, V, could be obtained whose positive and negative values correspond to the northeast and southwest directions; it also gives the cross-shore current, U, whose positive and negatives values correspond to the offshore and onshore directions, respectively.

mained at 17.0–19.5°C no matter whether the monsoon was in its relaxation or onset state. This indicates that the bottom layer of the corresponding area, rather than being affected by the cold CCC, is mainly controlled by the warm water of the CWC during the observation periods.

4.3 *Forcing mechanism of short term variation of subtidal currents*

Since previous studies (Jan et al., 2002; Lin et al., 2005; Zhu et al., 2013) generally consider that circulations in the western TWS are mainly controlled by the monsoons, here we use a vector empirical orthogonal function (VEOF) method (Hardy and Walton, 1978) to explore the connection between subtidal currents and wind. The subsequent discussion pertains to the first two modes of the VEOF analysis. This is primarily because the first two modes account for 88%, 93% and 91% of the total variance in the VEOF analysis for B3, B4, and B6, respectively.

Figure 6 displays the spatial structures and time-dependent

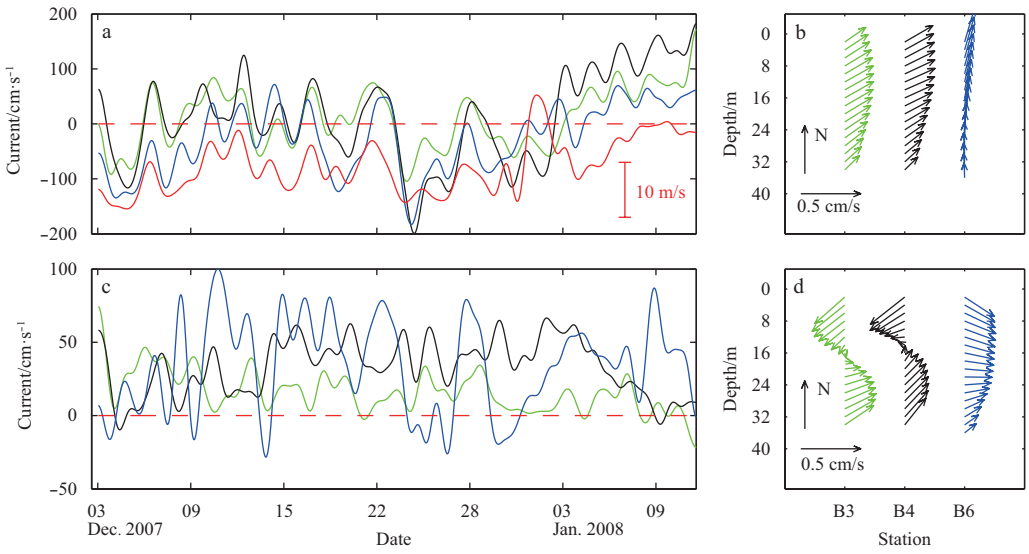

Fig. 6. Temporal (a) and spatial (b) mode of VEOF 1, and temporal (c) and spatial (d) modes of VEOF 2. The alongshore component of the wind is shown in Fig. 6a as a red curve. The green, black and blue curves correspond to Stations B3, B4 and B6, respectively.

coefficients for the first and second modes of the VEOF decomposition. The first VEOF mode (VEOF1) contains 60%, 77% and 79% of the total variance at B3, B4 and B6, respectively (Figs 6a and b). The spatial map for the VEOF1 (Fig. 6b) shows a generally uniform shear flow at all the sites, with a decline in velocity from the surface layer to the bottom layer (i.e., a quasi-barotropic structure of flow profile). The time coefficient for the VEOF1 (Fig. 6a) displays that it fluctuates with the northeasterly wind, with the correlation between it and the alongshore wind being 0.63, 0.62, and 0.76 at B3, B4, and B6, respectively. The spectral analysis shows an identical broad peak at a subtidal period around 2.0–5.0 d for the time coefficient of the VEOF1 and the alongshore wind (not shown). A significant coherence is found between them at this subtidal period with the flows lagging wind by about 0–5.7 h at the three sites (Figs 7a and b). This short, almost instantaneous, response of the flow to the alongshore wind

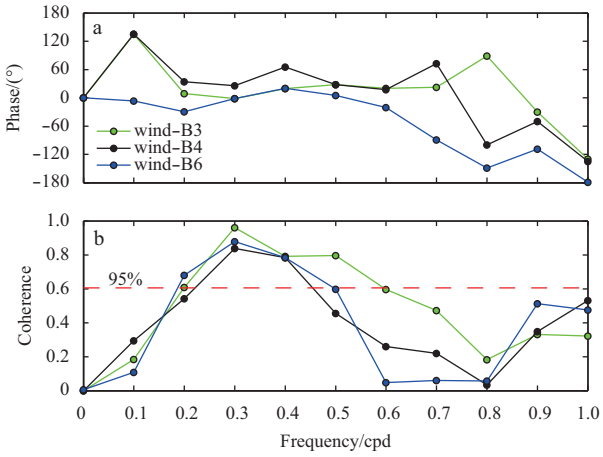

Fig. 7. The phase (a) and the coherence squared (b) between the first temporal VEOF mode and the alongshore component of the wind. The red dotted line in Fig. 7b represents the 95% significance level (0.61). The green, black and blue curves correspond to B3, B4 and B6 stations associated with the wind, respectively. 1 cpd=Hz/86 400.

is a typical case of a local, directly forced, wind-driven response (Chuang, 1985). Therefore, the temporal behavior for the VEOF1 (Figs 6a and b) mainly contributed to wind-driven quasibarotropic subtidal currents, showing a very strong short-term variation with a relatively strong northeastward flow (i.e., the CWC) over the whole water column in the western strait during the winter monsoon relaxation, which reverted to a succession of southwestward flow (i.e., the CCC) events as the northeasterly wind intensified, similar to the behavior shown in Fig. 5a. Obviously, the 2.0–5.0 d fluctuation of the northeasterly wind for driving the subtidal currents in the western strait is thought to be related to the periodic monsoon frontal passages (Chuang, 1986).

The second VEOF mode (VEOF2) contains 28%, 16% and 12% of the total variance at B3, B4 and B6, respectively (Figs 6c and d). Unlike the VEOF1, the spatial structure of the VEOF2 shows a typical baroclinic structure (Fig. 6d). At B3 and B4, the velocity vectors were southwestward (northeastward) above (below) the 16 m layer. Similar to B3 and B4, the velocity vectors at B6 were mainly southeastward from the surface layer to the 20 m layer, but were northeastward below the 20 m layer. As the VEOF2 time series show almost positive values in spite of very strong fluctuation at all sites during the observation periods, consequently, the second mode mainly contributed to persistent background currents with a two-layer structure in the western strait. That is to say, in the upper layer, there was a uniform southward background current driven by the winter monsoon; in the bottom layer, there exists a steady northeastward current throughout the western strait, which is thought to be primarily caused by an alongshore sea level slope (Fang and Zhao, 1988; Yang, 2007).

Therefore, the variation of spatial extension for the CWC and the CCC in the western strait shown in Fig. 5, was mainly controlled by the first mode and slightly modulated by the second mode. As the northeasterly wind intensified, the wind-driven strong downwind currents (Figs 6a and b) overlapped with the relatively weak background current (Figs 6c and d), leading to a stronger along-strait downwind current (i.e., the CCC, Figs 5b–d), with a larger extension in space in the western TWS. In contrast, when the monsoon became weak, similar processes operated but in an opposite direction.

5 Conclusions

In the past few decades, the current characteristics of the TWS in winter had received much attention and there are many achievements (e.g., Lin et al., 2005; Guan and Fang, 2006; Yang, 2007; Liao et al., 2013; Oey et al., 2014). However, due to the paucity of synchronous or quasi-synchronous measurements corresponding to different states of the winter monsoon, the spatio-temporal variation of current patterns in the strait is still poorly understood. In the present study, the subtidal currents are explored by a new set of the SADCP and BADCP observations, which were collected in the winter seasons of recent years. To extract the subtidal currents, the least squares method is employed to separate tides from the SADCP measurements. It is worth mentioning that the spatial distribution characteristics of M_2 tidal current obtained from the SADCP observations agree well with the results of the ADCIRC model, which are also consistent with previous works. In this study, we confirm the existence of the intense cotidal lines for M_2 tidal current, which is located north of 25°N; meanwhile, it should also be noted that in our case no existence of the amphidromic point is observed.

Our results indicate that the flow pattern in the western portion of the TWS is rather different between the relaxation and break stages of the winter monsoon. The CWC could extend through the whole western strait and even occupied the entire water column during the winter monsoon relaxation stage. However, when the winter monsoon outbreak started, the intense northeasterly wind forced the along-strait current to flow downwind in the western strait, while the northeastward CWC was very weak and only existed in the subsurface and bottom layers. Particularly, the CWC was almost overwhelmed during the two big monsoon bloom events in the winter of 2007, and as a result, the whole water column was dominated by the strong CCC throughout the western strait. The VEOF result indicated that the variation of spatial extent of the CWC and the CCC in the western strait was mainly controlled by a wind-driven quasi-barotropic current as the first mode and slightly modulated by a relatively weak background current with a first-order baroclinic structure as the second mode.

Although the local wind played a dominant role in the fluctuation of the subtidal currents in the western TWS, it could not be the only important factor. It shall be noted that since the CWC is against the winter monsoon, the CWC is most likely driven by the pressure gradient, as noted in some previous studies (Chuang, 1985; Yang, 2007). However, up to date it remains unclear whether the corresponding cross-strait component or the along-strait one plays the dominating role. To answer this question, in addition to the simulation method, synchronous in-site sea level records observed in a CWC-bloom event during the winter monsoon, if there are any, are expected to contribute a lot to explaining the driving mechanism of the CWC and will be reported in our future work.

Acknowledgements

The authors acknowledge the officers and crew of the mooring cruises and the managers of the ships for their support. They are grateful to the European Centre for Medium-range Weather Forecasts (ECMWF) for providing their reanalysis wind product (http://apps.ecmwf.int/datasets/data/interim_ full_daily/).

References

Candela J, Beardsley R C, Limeburner R. 1992. Separation of tidal and subtidal currents in ship-mounted acoustic Doppler current profiler observations. Journal of Geophysical Research, 97(C1): 769–788

Chen C T A. 2003. Rare northward flow in the Taiwan Strait in winter: a note. Continental Shelf Research, 23(3–4): 387–391

Chiao L Y, Wang Yuhuai. 2004. Multiresolution interpolation and detiding of the ADCP data. Journal of Atmospheric and Oceanic Technology, 21(1): 122–134

Chuang W S. 1985. Dynamics of subtidal flow in the Taiwan Strait. Journal of the Oceanographical Society of Japan, 41(2): 65–72

Chuang W S. 1986. A note on driving mechanism of the current in the Taiwan Strait. Journal of Oceanography, 42(5): 355–361

Fang Guohong, Yang Jingfei, Zhao Xucai. 1985. A numerical model for tides and tidal currents in the Taiwan Strait. Acta Oceanologica Sinica (in Chinese), 7(1): 12–20

Fang Guohong, Zhao Baoren. 1988. A note on the main forcing of the northeastward flowing current off the southeast China coast. Progress in Oceanography, 21(34): 363–372

Geyer W R, Signell R. 1990. Measurements of tidal flow around a headland with a shipboard acoustic Doppler current profiler. Journal of Geophysical Research, 95(C3): 3189–3197

Guan Bingxian. 1986. Evidence for a counter-wind current in winter off the southeast coast of China. Chinese Journal of Oceanology and Limnology, 4(4): 319–332

Guan Bingxian, Fang Guohong. 2006. Winter counter-wind currents off the southeastern China coast: a review. Journal of Oceanography, 62(1): 1–24

Hardy D M, Walton J J. 1978. Principal components analysis of vector wind measurements. Journal of Applied Meteorology, 17(8): 1153–1162

Hsueh Y, Romea R D. 1983. A comparison of observed and geostrophically calculated winter time surface winds over the East China Sea. Journal of Geophysical Research, 88(C14): 9588–9594

Hu Jianyu, Fu Zilang, Wu Lianxing. 1990. Studies on the wintertime current structure and T-S fine-structure in the Taiwan Strait. Chinese Journal of Oceanology and Limnology, 8(4): 319–327

Hu Jianyu, Kawamura H, Li Chunyan, et al. 2010. Review on current and seawater volume transport through the Taiwan Strait. Journal of Oceanography, 66(5): 591–610

Isobe A, Kuramitsu T, Nozaki H, et al. 2007. Reliability of ADCP data detided with a numerical model on the East China Sea shelf. Journal of Oceanography, 63(1): 135–141

Jan S, Chern C S, Wang J, et al. 2004. The anomalous amplification of M_2 tide in the Taiwan Strait. Geophysical Research Letters, 31(7): doi: 10.1029/2003GL019373

Jan S, Sheu D D, Kuo H M. 2006. Water mass and through flow transport variability in the Taiwan Strait. Journal of Geophysical Research, 111(C12): C12012, doi: 10.1029/2006JC003656

Jan S, Wang J, Chern C S, et al. 2002. Seasonal variation of the circulation in the Taiwan Strait. Journal of Marine System, 35(34): 249–268

Ko D S, Preller R H, Jacobs G A, et al. 2003. Transport reversals at Taiwan Strait during October and November 1999. Journal of Geophysical Research, 108(C11): doi: 10.1029/2003JC001836

Kuang Fangfang, Zhang Youquan, Zhang Junpeng, et al. 2015. Comparison and evaluation of three sea surface wind products in Taiwan Strait. Haiyang Xuebao (in Chinese), 37(5): 44–53

Kundu P K, Allen J S. 1976. Some three-dimensional characteristics of low-frequency current fluctuations near the Oregon coast. Journal of Physical Oceanography, 6(2): 181–199

Li Li. 1986. Annual wind variation in the coasts along Taiwan Strait. Taiwan Strait (in Chinese), 5(2): 107–113

Li Li, Wang Shoujing. 1990. Notes on tidal current in the Taiwan Strait. Oceanologia et Limnologia Sinica (in Chinese), 21(6): 578–580

Liang W D, Tang T Y, Yang Y J, et al. 2003. Upper-ocean currents around Taiwan. Deep-Sea Research: Part II, 50(67): 1085–1105

Liao Enhui, Jiang Yuwu, Li Li, et al. 2013. The cause of the 2008 cold disaster in the Taiwan Strait. Ocean Modelling, 62: 1–10

Limeburner R. 1985. CODE-2: moored array and large-scale data report. WHOI Technical Report WHOI85-35. Woods Hole, Mass: Woods Hole Oceanographic Institution

Lin S F, Tang T Y, Jan S, et al. 2005. Taiwan Strait current in winter. Continental Shelf Research, 25(9): 1023–1042

Münchow A. 2000. Detiding three-dimensional velocity survey data in coastal waters. Journal of Atmospheric and Oceanic Technology, 17(5): 736–748

Oey L Y, Chang Y L, Lin Y C, et al. 2014. Cross flows in the Taiwan Strait in winter. Journal of Physical Oceanography, 44(3): 801–817

Pan Aijun, Wan Xiaofang, Guo Xiaogang, et al. 2013. Responses of the Zhe-Min coastal current adjacent to Pingtan Island to the wintertime monsoon relaxation in 2006 and its mechanism. Science China Earth Science, 56(3): 386–396

Qiu Yun, Li Li, Chen C T A, et al. 2011. Currents in the Taiwan Strait as observed by surface drifters. Journal of Oceanography, 67(4): 395–404

Su Jilan, Wang Wei. 1987. On the sources of the Taiwan Warm Current from the South China Sea. Chinese Journal of Oceanology and Limnology, 5(4): 299–308

Sun Xiangping, Su Yufen, Xiu Shumeng. 1996. Current in the offshore areas east and west of Taiwan. Journal of Oceanography of Huanghai and Bohai Seas (in Chinese), 14(2): 9–17

Takikawa T, Yoon J H, Cho K D. 2003. Tidal currents in the Tsushima Straits estimated from ADCP data by ferryboat. Journal of Oceanography, 59(1): 37–47

Tseng R S, Shen Y T. 2003. Lagrangian observations of surface flow patterns in the vicinity of Taiwan. Deep-Sea Research: Part II, 50(67): 1107–1115

Vazquez H J, Gomez-Valdes J, Ortiz M. 2011. Detiding shipboard ADCP data in eastern boundary current. Journal of Atmospheric and Oceanic Technology, 28(1): 94–103

Wang Yuhuai, Chiao L Y, Lwiza K M M, et al. 2004. Analysis of flow at the gate of Taiwan Strait. Journal of Geophysical Research, 109(C2): C02025, doi: 10.1029/2003JC001937

Wang Dongxiao, Hong Bo, Gan Jianping, et al. 2010. Numerical investigation on propulsion of the counter-wind current in the northern South China Sea in winter. Deep-Sea Research: Part I, 57(10): 1206–1221

Wang Yuhuai, Jan S, Wang Dongping. 2003. Transports and tidal current estimates in the Taiwan Strait from shipboard ADCP observations (1999–2001). Estuarine, Coastal and Shelf Science, 57(12): 193–199

Westerink J J, Luettich R A, Scheffner N. 1993. ADCIRC: an advanced three-dimensional circulation model for shelves, coasts, and estuaries. Report 3. Development of a tidal constituent database for the western north Atlantic and Gulf of Mexico. DRP Technical Report DRP-92-6. Ms: Vicksburg Department of the Army, US Army Corps of Engineers, Waterways Experiment Station

Wu C R, Chao S Y, Hsu C. 2007. Transient, seasonal and interannual variability of the Taiwan Strait current. Journal of Oceanography, 63(5): 821–833

Xiao Hui, Cai Shuhui. 1988. Distribution characters of sea temperature and salinity in western Taiwan Strait. Journal of Oceanography in Taiwan Strait (in Chinese), 7(3): 227–234

Yang Jiayan. 2007. An oceanic current against the wind: how does Taiwan island steer warm water into the East China Sea?. Journal of Physical Oceanography, 37(10): 2563–2569

Ye Anle, Chen Zongyong, Yu Yifa. 1985. Numerical inverstigation of three-dimensional semidiurnal tidal waves in Taiwan Strait and its adjacent areas. Oceanologia et Limnologia Sinica (in Chinese), 16(6): 439–450

Zhang Caiyun, Shang Shaoling, Chen Dewen, et al. 2005. Short-term variability of the distribution of Zhe-Min coastal water and wind forcing during winter monsoon in the Taiwan Strait. Journal of Remote Sensing (in Chinese), 9(4): 452–458

Zhang Yiken, Weng Xuechuan, Zhang Qilong, et al. 1991. Bottom current in Taiwan Strait. Oceanologia et Limnologia Sinica (in Chinese), 22(2): 124–131

Zhu Dayong, Li Li, Guo Xiaogang. 2013. Seasonal and interannual variations of surface current in the southern Taiwan Strait to the west of Taiwan Shoals. Chinese Science Bulletin, 58(33): 4171–4178